INTERNATIONAL JOURNAL FOR NUMERICAL METHODS IN FLUIDS
Int. J. Numer. Meth. Fluids 2006; **51**:749–771
Published online 20 December 2005 in Wiley InterScience (www.interscience.wiley.com). DOI: 10.1002/fld.1146

A stable second-order mass-weighted upwind scheme for unstructured meshes

Luu Dung Tran[‡,¶], Christian Masson[*,†,‖] and Arezki Smaïli[§,**]

Department of Mechanical Engineering, École de Technologie Supérieure, Montréal, Canada

SUMMARY

In this paper, an original second-order upwind scheme for convection terms is described and implemented in the context of a Control-Volume Finite-Element Method (CVFEM).

The proposed scheme is a second-order extension of the first-order MAss-Weighted upwind (MAW) scheme proposed by Saabas and Baliga (*Numer. Heat Transfer* 1994; **26B**:381–407). The proposed second-order scheme inherits the well-known stability characteristics of the MAW scheme, but exhibits less artificial viscosity and ensures much higher accuracy. Consequently, and in contrast with nearly all second-order upwind schemes available in the literature, the proposed second-order MAW scheme does not need limiters.

Some test cases including two pure convection problems, the driven cavity and steady and unsteady flows over a circular cylinder, have been undertaken successfully to validate the new scheme.

The verification tests show that the proposed scheme exhibits a low level of artificial viscosity in the pure convection problems; exhibits second-order accuracy for the driven cavity; gives accurate reattachment lengths for low-Reynolds steady flow over a circular cylinder; and gives constant-amplitude vortex shedding for the case of high-Reynolds unsteady flow over a circular cylinder. Copyright © 2005 John Wiley & Sons, Ltd.

KEY WORDS: CVFEM; second-order upwind scheme

*Correspondence to: Christian Masson, Department of Mechanical Engineering, École de Technologie Supérieure, 1100 Notre-Dame West, Montréal, Québec, Canada H3C 1K3.
†E-mail: christian.masson@etsmtl.ca
‡E-mail: ltran@etsmtl.ca
§E-mail: asmaili@etsmtl.ca
¶Post-Doctoral student.
‖Professor, Holder of the Canada Research Chair on the Aerodynamics of Wind Turbines in Nordic Environment.
**Research scientist.

Contract/grant sponsor: Canada Research Chair Program
Contract/grant sponsor: Ministère des ressources naturelles du Québec
Contract/grant sponsor: Canadian Natural Resources Ministry
Contract/grant sponsor: Natural Sciences and Engineering Research Council of Canada

Received 25 October 2004
Revised 13 September 2005
Accepted 21 September 2005

1. INTRODUCTION

Since the original development of the control-volume finite-element method (CVFEM) by Baliga and Patankar [1], CVFEMs have been developed, implemented and applied to various flow phenomena by many authors [2–11]. This method is attractive, as it combines the mesh flexibility of a finite-element approach with the physically meaningful formulation of the control-volume method. With the proposition of the equal-order co-located scheme of Prakash and Patankar [3], which permitted the calculation of pressure and velocity at the same nodes, CVFEMs became easier to implement and use. The introduction, by Saabas and Baliga [4] and Masson *et al.* [5], of the MAss-Weighted upwind scheme (MAW), which is an adaptation for tetrahedral and triangular elements of the skewed positive influence coefficient upwind scheme of Schneider and Raw [12], significantly improved the CVFEM's stability characteristics and applicability range. However, these first-order upwind schemes [4, 5, 12] can produce high levels of artificial viscosity, especially when flow direction is not aligned with the grid and in cases of unsteady flows [13]. For example, the first-order MAW scheme applied to the unsteady flows over a circular cylinder does not yield satisfactory results. The artificial viscosity introduced by discretization errors causes Von-Karman vortices behind a circular cylinder to decay and then disappear in the case of unsteady flow at $Re = 100$. In the cases of steady flows with Reynolds numbers lower than 40, the first-order MAW scheme predicts a much shorter reattachment length than expected.

Many variations of high-order schemes for convection terms on unstructured mesh have been proposed [14, 15]. Following the MAW scheme principle to ensure stability, an original second-order upwind scheme for convection terms is proposed, implemented and validated in this paper. The results obtained with the new scheme on five test cases (two pure convection problems, the driven cavity, steady and unsteady laminar flows over a circular cylinder) give highly conclusive results.

2. GOVERNING EQUATIONS

The system of conservation equations for an incompressible flow in a control volume V enclosed by a surface A can be written in the following integral form:

1. *Continuity equation*

$$\oint_A \rho(\mathbf{V}^m \cdot \mathbf{n})\,\mathrm{d}A = 0 \tag{1}$$

2. *Momentum equation along the x_i-axis*

$$\frac{\partial}{\partial t}\int_V \rho u_i\,\mathrm{d}V + \oint_A \rho u_i(\mathbf{V}^m \cdot \mathbf{n})\,\mathrm{d}A = -\int_V \frac{\partial p}{\partial x_i}\,\mathrm{d}V + \oint_A \mu(\nabla u_i \cdot \mathbf{n})\,\mathrm{d}A \tag{2}$$

3. *General scalar transport equation*

$$\frac{\partial}{\partial t}\int_V \rho\phi\,\mathrm{d}V + \oint_A \rho\phi(\mathbf{V}^m \cdot \mathbf{n})\,\mathrm{d}A = \oint_A \Gamma_\phi(\nabla\phi \cdot \mathbf{n})\,\mathrm{d}A + \int_V S_\phi\,\mathrm{d}V \tag{3}$$

where ϕ is the general transported and dependent variable; $\mathbf{V}^m$ is the mass-flux (or convecting) velocity whose components are determined by Equation (10); u_i is the component along the x_i-axis of convected velocity $\mathbf{u}$; $\mathbf{n}$ is the outward unit vector normal to the elementary surface $\mathrm{d}A$; ρ, μ are the fluid density and viscosity; $\partial p/\partial x_i$ is the component along the axis x_i of pressure gradient; Γ_ϕ is the diffusion coefficient of the general transported variable ϕ, and S_ϕ is the source term of ϕ per unit volume.

3. NUMERICAL METHOD

The CVFEM used in this paper is based on the formulation presented in Reference [5]. Only the aspects needed to understand the proposed second-order MAW scheme are presented in this paper. The reader interested in a complete description of the CVFEM should consult Reference [5].

3.1. Discretization

During the discretization procedure, the finite-volume technique is used to convert the above-mentioned equations into a system of algebraic equations. The governing equations are discretized and integrated over the control volume (CV) surrounding each node to obtain discrete equations expressing the conservation of convected quantities in the control volume.

In the CVFEM, the unstructured mesh inherited from the finite-element approach is used in a co-located equal-order scheme. The spatial discretization procedure is based on triangular elements at whose vertices all variables and pressure are stored. A polygonal control volume (see Figure 1) around each node is formed by connecting the midpoints of the edges departing from a given node **c** to the centroids of neighbouring triangular elements. The temporal discretization is based on a first-order Euler scheme with a fully-implicit unsteady formulation.

3.1.1. General scalar transport equation. In integral form, the conservation equation for a general transported scalar ϕ in the control volume around node **c** (see Figure 1) can be

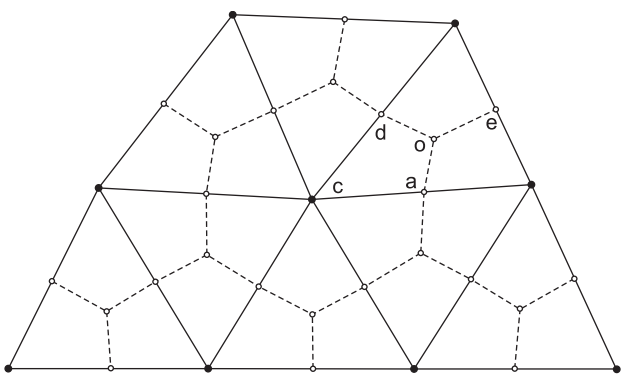

Figure 1. Unstructured mesh based on triangular elements.

written as

$$\int_a^o (\mathbf{J}_D + \mathbf{J}_C)\cdot\mathbf{n}\,dA + \int_o^d (\mathbf{J}_D + \mathbf{J}_C)\cdot\mathbf{n}\,dA - \int_{caod} S_\phi\,dV + \int_{caod} \frac{\partial}{\partial t}(\rho\phi)\,dV$$
$$+ (\text{Similar contributions from other elements associated with node } \mathbf{c})$$
$$+ (\text{Boundary contributions, if applicable}) = 0 \tag{4}$$

where $\mathbf{J}_C = \rho\mathbf{V}^m\phi$ and $\mathbf{J}_D = -\Gamma_\phi\cdot\nabla\phi$ are the convection and diffusion fluxes, respectively.

In this formula, only the contributions from one triangular element (i.e. from the subcontrol volume **caod** in Figure 1) are presented explicitly. The contributions for the other elements associated with node **c** are determined in a similar manner.

Based on this formula, an 'element-by-element' assembling procedure can be used to construct the discretized conservation equation of ϕ in the control volume around each node, which can be cast in the following general representation:

$$a^\phi\phi - \sum_{nb} a_{nb}^\phi\phi_{nb} = b^\phi \tag{5}$$

where a^ϕ is the coefficient of the central node **c** and a_{nb}^ϕ are the coefficients of its neighbour nodes.

3.1.2. Momentum equations. The momentum equation is obtained from Equation (4), when ϕ corresponds to the velocity component u_i along the axis x_i and S_ϕ is the pressure gradient

$$a^{u_i}u_i - \sum_{nb} a_{nb}^{u_i}(u_i)_{nb} = b^{u_i} - V_{CV}\left(\frac{\partial p}{\partial x_i}\right)_{CV} \tag{6}$$

or

$$u_i = \hat{u}_i - d_i^{u_i}\left(\frac{\partial p}{\partial x_i}\right)_{CV} \tag{7}$$

where

$$\hat{u}_i = \frac{\sum_{nb} a_{nb}^{u_i}(u_i)_{nb} + b^{u_i}}{a^{u_i}} \tag{8}$$

and

$$d_i^{u_i} = \frac{V_{CV}}{a^{u_i}} \tag{9}$$

To prevent the occurrence of spurious pressure oscillations in the adopted co-located equal-order formulation, following Rhie and Chow's proposition [16], the mass flux should always be evaluated using a velocity component u_i^m 'staggered' from the 'convected' velocity component u_i computed from the discretized momentum equation (Equation (6)).

Velocity $\mathbf{V}^m$ is called the 'mass-flux' or 'convecting' velocity. Its components are computed from the momentum equation (Equation (7)) but using the pressure gradient at the element level instead of using the control-volume pressure gradient

$$u_i^m = \hat{u}_i - d^{u_i}\left(\frac{\partial p}{\partial x_i}\right)_{ele} \tag{10}$$

For the evaluation of the 'mass-flux' velocity components on the faces a–o and o–d (see Figure 1), $\hat{u}_i$ and $d_i^{u_i}$ are interpolated linearly from the corresponding values at the vertices of the element.

3.1.3. Equation for pressure. By substituting the mass velocity determined by Equation (10) in the continuity equation (Equation (1)), the discretized equation for pressure is obtained. It has the same form as Equation (5).

$$a^p p - \sum_{nb} a_{nb}^p p_{nb} = b^p \tag{11}$$

3.2. Boundary conditions

3.2.1. Dirichlet boundary conditions. On boundaries where the values of a variable ϕ are specified, the following procedure is applied:

$$a^\phi = 1; \quad a_{nb}^\phi = 0; \quad b^\phi = \phi_{\text{sp}} \tag{12}$$

3.2.2. Neumann boundary conditions. When the gradient $\partial\phi/\partial n$ is specified on a boundary, the flux of ϕ through the boundary surface is calculated from the given gradient $\partial\phi/\partial n$ and then added to the balance of ϕ in the corresponding CV near the boundary.

3.2.3. Special treatment of BC for pressure equation. Some special treatments are needed on boundaries with prescribed velocities. In the CVFEM proposed by Masson *et al.* [5], the d^{u_i} are set to zero at such nodes, and therefore

$$\hat{u} = u_{\text{specified}} \quad \text{and} \quad d^{u_i} = 0 \tag{13}$$

However, in control volumes where the central node and all its neighbours lie on such boundaries, the central coefficient a^p of the pressure equation is reduced to zero, since a^p is proportional to d^{u_i}. Consequently, the presence of such coefficients can lead to physically unrealistic solutions.

To avoid this problem, as proposed by Smaïli and Masson [17], the values of d^{u_i} and $\hat{u}_i$, at nodes where the velocity is specified, are calculated using Equation (9) and the momentum balance of their control volume (Equation (7))

$$\hat{u}_i = u_{\text{specified}} + d^{u_i} \left(\frac{\partial p}{\partial x_i} \right)_{\text{CV}} \tag{14}$$

4. FLO AND MAW SCHEMES FOR CONVECTION

In research done by Saabas and Baliga [4] and Masson *et al.* [5], two interpolation schemes were used to evaluate the convection fluxes: FLow Oriented (FLO) and MAss Weighted (MAW) schemes.

In the FLO scheme, the combination of exponential interpolation and the use of local coordinate systems in each triangular element with axis parallel to the local flow direction [1]

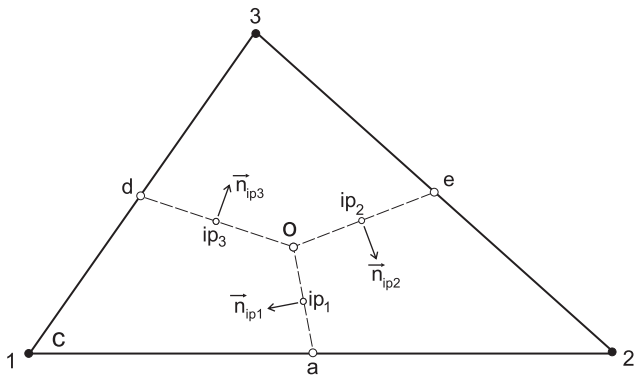

Figure 2. Elementary triangular element.

made it an accurate convection scheme on unstructured meshes. The weakness of the FLO scheme is its stability. For complex flow configurations, it is difficult to achieve convergence: when high element Peclet numbers are encountered, the FLO scheme can lead to negative coefficients in algebraic discretized equations, and this difficulty is compounded when obtuse-angled triangular elements are used [5].

The first-order MAW scheme [4, 5] is quite stable and is often used to calculate complex flows. MAW has acceptable accuracy for simple flow configurations, but it produces a considerable level of artificial viscosity when the mesh is not parallel to the flow direction, especially for unsteady flows.

The proposed second-order MAW scheme inherits the main advantage of the MAW scheme—its stability—but ensures much higher accuracy. Since the proposed second-order scheme is based on the first-order MAW scheme, a complete description of the MAW scheme follows.

4.1. The original MAW scheme

The original idea for the MAW scheme was proposed by Schneider and Raw [12] as a skewed positive influence coefficient upwinding scheme and has been adapted for tetrahedral elements by Saabas and Baliga [4] and for triangular elements by Masson *et al.* [5].

Figure 2, illustrating a typical triangular element, indicates the notation convention for vertex nodes (1, 2, and 3), the integration points for the evaluation of the convection fluxes (ip_1, ip_2, and ip_3), and the sign convention for the unit normals at control surfaces ($\mathbf{n}_{ip_1}$, $\mathbf{n}_{ip_2}$, and $\mathbf{n}_{ip_3}$).

The MAW scheme defines a mass-weighted average of ϕ at the integration point of each of the three control surfaces of a triangular element (Figure 2), namely, ϕ_{ip_1}, ϕ_{ip_2}, ϕ_{ip_3}, in the following manner: Let

$$\dot{m}_{ip_1} = \int_a^o \rho \mathbf{V}^m \cdot \mathbf{n}_{ip_1} \, dA; \quad \dot{m}_{ip_2} = \int_e^o \rho \mathbf{V}^m \cdot \mathbf{n}_{ip_2} \, dA; \quad \dot{m}_{ip_3} = \int_d^o \rho \mathbf{V}^m \cdot \mathbf{n}_{ip_3} \, dA \tag{15}$$

The value of a convected quantity at an integration point, for example at ip_1 on the edge **oa** of the CV boundary around node 1, is calculated as (see Figure 2)

$$\phi_{\mathrm{ip}_1} = A_1.[f_{1_R}.\phi_{\mathrm{ip}_2} + (1 - f_{1_R}).\phi_2] + (1 - A_1).[f_{1_L}.\phi_{\mathrm{ip}_3} + (1 - f_{1_L}).\phi_1] \tag{16}$$

where

$$A_1 = \begin{cases} 1 & \text{if } \dot{m}_{\mathrm{ip}_1} > 0 \text{ (i.e. the flow through edge } \mathbf{oa} \text{ originates from its right side)} \\ 0 & \text{if } \dot{m}_{\mathrm{ip}_1} < 0 \text{ (i.e. the flow through edge } \mathbf{oa} \text{ originates from its left side)} \end{cases}$$

When the mass flux through edge **oa** originates from its right side, i.e. from ip_2 and/or from node 2, then $\dot{m}_{\mathrm{ip}_1} > 0$, $A_1 = 1$ and only the first member of the RHS of Equation (16) is used with the weighting factor f_{1_R}, determined as

$$f_{1_R} = \begin{cases} 1 & \text{if } \dot{m}_{\mathrm{ip}_2} > \dot{m}_{\mathrm{ip}_1} > 0 \\ \dfrac{\dot{m}_{\mathrm{ip}_2}}{\dot{m}_{\mathrm{ip}_1}} & \text{if } \dot{m}_{\mathrm{ip}_1} > \dot{m}_{\mathrm{ip}_2} > 0 \\ 0 & \text{if } \dot{m}_{\mathrm{ip}_1} > 0 > \dot{m}_{\mathrm{ip}_2} \end{cases} \tag{17}$$

The weighting factor f_{1_R} is used to interpolate ϕ_{ip_1} as a linear function of ϕ_{ip_2} and ϕ_2, depending on the ratio of mass fluxes coming from the integration point ip_2 and node 2. This weighting factor is used to distinguish among three situations:

1. If $\dot{m}_{\mathrm{ip}_2} > \dot{m}_{\mathrm{ip}_1} > 0$, the mass flux through edge **oe** flows to both ip_1 and node 2. With $f_{1_R} = 1$, from Equation (16), ϕ_{ip_1} is taken as equal to the upwind value: $\phi_{\mathrm{ip}_1} = \phi_{\mathrm{ip}_2}$.
2. If $\dot{m}_{\mathrm{ip}_1} > \dot{m}_{\mathrm{ip}_2} > 0$, the resulting mass flux $\dot{m}_{\mathrm{ip}_1}$ partly originates from ip_2 and from node 2. The weighting factor $f_{1_R} = \dot{m}_{\mathrm{ip}_2}/\dot{m}_{\mathrm{ip}_1}$ allows us to interpolate ϕ_{ip_1} from its upwind values ϕ_{ip_2} and ϕ_2.
3. If $\dot{m}_{\mathrm{ip}_1} > 0 > \dot{m}_{\mathrm{ip}_2}$, the mass flux flows from node 2 to both ip_1 and ip_2. So $f_{1_R} = 0$ ensures $\phi_{\mathrm{ip}_1} = \phi_2$.

When the mass flux at ip_1 originates from the left side of edge **oa**, i.e. from ip_3 and/or node 1, $\dot{m}_{\mathrm{ip}_1} < 0$, $A_1 = 0$ only the second member of RHS of Equation (16) is used to interpolate ϕ_{ip_1} in a similar manner.

Finally, by writing Equation (16) for three integration points in a triangular element, a system of three linear equations for three unknowns ϕ_{ip_1}, ϕ_{ip_2}, ϕ_{ip_3} is obtained

$$\begin{aligned} \phi_{\mathrm{ip}_1} - A_1.f_{1_R}.\phi_{\mathrm{ip}_2} - (1 - A_1).f_{1_L}.\phi_{\mathrm{ip}_3} &= A_1.[(1 - f_{1_R}).\phi_2] \\ &\quad + (1 - A_1).[(1 - f_{1_L}).\phi_1] \\ -(1 - A_2).f_{2_L}.\phi_{\mathrm{ip}_1} + \phi_{\mathrm{ip}_2} - A_2.f_{2_R}.\phi_{\mathrm{ip}_3} &= A_2.[(1 - f_{2_R}).\phi_3] \\ &\quad + (1 - A_2).[(1 - f_{2_L}).\phi_2] \\ -A_3.f_{3_R}.\phi_{\mathrm{ip}_1} - (1 - A_3).f_{3_L}.\phi_{\mathrm{ip}_2} + \phi_{\mathrm{ip}_3} &= A_3.[(1 - f_{3_R}).\phi_1] \\ &\quad + (1 - A_3).[(1 - f_{3_L}).\phi_3] \end{aligned} \tag{18}$$

This system can be easily solved to find the values of convected parameter at three integration points as function of the values ϕ_1, ϕ_2, ϕ_3 at vertices of the triangular element and of the mass fluxes $\dot{m}_{\mathrm{ip}_1}$, $\dot{m}_{\mathrm{ip}_2}$, $\dot{m}_{\mathrm{ip}_3}$.

These mass-weighted averages of ϕ are assumed to prevail over each control surface when the surface integrals of the convection terms, Equation (4), are evaluated. Consequently, the convection contributions are simply expressed as

$$\int_a^o \mathbf{J}_{\mathrm{C}} \cdot \mathbf{n}\, \mathrm{d}A = -\dot{m}_{\mathrm{ip}_1} \phi_{\mathrm{ip}_1} \tag{19}$$

$$\int_o^d \mathbf{J}_{\mathrm{C}} \cdot \mathbf{n}\, \mathrm{d}A = \dot{m}_{\mathrm{ip}_3} \phi_{\mathrm{ip}_3} \tag{20}$$

It should be noted that $\dot{m}_{\mathrm{ip}_1}$ and $\dot{m}_{\mathrm{ip}_3}$ are mass flow rates across the corresponding control surfaces, in the directions of the normals $\mathbf{n}_{\mathrm{ip}_1}$ and $\mathbf{n}_{\mathrm{ip}_3}$, respectively (see Figure 2).

The algebraic approximation to the elemental convection contribution can be compactly expressed as follows:

$$\int_a^o \mathbf{J}_{\mathrm{C}} \cdot \mathbf{n}\, \mathrm{d}A + \int_o^d \mathbf{J}_{\mathrm{C}} \cdot \mathbf{n}\, \mathrm{d}A = C_1^{\phi} \phi_1 + C_2^{\phi} \phi_2 + C_3^{\phi} \phi_3 \tag{21}$$

Expressions similar to Equation (21) can be derived for the convection contributions of all elements associated with the internal node **c** shown in Figure 2. Such expressions, when substituted into Equation (4), yield the complete convection contribution to the discretization equation for node **c** (Equation (5)).

Equations (18) explain how the value of ϕ at an integration point is interpolated from the values at its two upwind points using the mass flux through the three integration points. At the same time, it ensures the 'skewed' and 'positive influence-coefficient' characteristics of the original MAW scheme:

1. The transported quantity ϕ at each integration point is interpolated from the values of its two upwind points: an upwind integration point and an upwind node. The 'skewness' characteristic is manifested by flexibly interpolating the values at two upstream positions: the upwind points are not fixed rigidly by the grid (as in the unidirectional upwind scheme, for example) but are taken as closely as possible to the upstream nodes along streamlines.
2. Secondly, Equations (18) ensure, at the element level, that the extent to which the dependent variable at a node exterior to a control-volume contributes to the convective outflow is less than or equal to its contribution to the inflow by convection. Thus, it is a sufficient condition for ensuring that the algebraic approximations to the convective terms add positively to the discretized equation [5], which guarantees numerical stability.

Briefly, the use of a flexible 'skewed' choice of upwind nodes in a 'positive coefficient' balance of convected quantities makes the original MAW scheme very stable and relatively accurate.

5. SECOND-ORDER SCHEMES FOR CONVECTION

5.1. Second-order versus first-order

Generally, in second-order schemes, to calculate the value ϕ_{ip} of a transported quantity at an integration point, the linear variation of ϕ from an upwind point to the integration point is assumed. The linear variation of ϕ from an upwind node to an integration point is calculated as the scalar product of the gradient of ϕ at the upwind node and the displacement vector between these two points

$$\phi_{\text{ip}} = \phi_{\text{UpwindNode}} + \nabla\phi_{\text{UpwindNode}}.\,\mathbf{\Delta r}_{\text{UpwindNode}\to\text{ip}} + \mathcal{O}((\Delta s)^2) \tag{22}$$

This is more accurate than in the first-order upwind scheme, where the value of ϕ_{ip} at an integration point is simply taken as equal to the value of its upwind point

$$\phi_{\text{ip}} = \phi_{\text{UpwindNode}} + \mathcal{O}(\Delta s)$$

In summary, the piecewise variation of ϕ in the first-order scheme is replaced by the linear variation in the second-order scheme, increasing the order of the truncation error from $\mathcal{O}(\Delta s)$ in the first-order scheme (here Δs is the mesh size) to $\mathcal{O}((\Delta s)^2)$ in the second-order scheme.

5.2. New second-order MAW scheme

Equation (16) is the basis of the first-order MAW scheme. In order to construct a second-order scheme having the skewness and positive-influence coefficient characteristics of the MAW scheme, the stepwise variation of ϕ assumed in Equation (16) has to be replaced by a piecewise-linear variation. This leads to the following expression:

$$\begin{aligned}\phi^{\text{2nd}}_{\text{ip}_1} = {} & A_1.[f_{1_R}.(\phi^{\text{2nd}}_{\text{ip}_2} + \Delta\phi_{\text{ip}_2\to\text{ip}_1}) + (1 - f_{1_R}).(\phi_2 + \Delta\phi_{\text{node}_2\to\text{ip}_1})] \\ & + (1 - A_1).[f_{1_L}.(\phi^{\text{2nd}}_{\text{ip}_3} + \Delta\phi_{\text{ip}_3\to\text{ip}_1}) + (1 - f_{1_L}).(\phi_1 + \Delta\phi_{\text{node}_1\to\text{ip}_1})]\end{aligned} \tag{23}$$

where

$$\Delta\phi_{\text{ip}_2\to\text{ip}_1} = (\nabla\phi)_{\text{ele}}.\mathbf{\Delta r}_{\text{ip}_2-\text{ip}_1} \tag{24}$$

$$\Delta\phi_{\text{ip}_3\to\text{ip}_1} = (\nabla\phi)_{\text{ele}}.\mathbf{\Delta r}_{\text{ip}_3-\text{ip}_1} \tag{25}$$

and

$$\Delta\phi_{\text{node}_2\to\text{ip}_1} = \nabla\phi_2.\mathbf{\Delta r}_{\text{node}_2-\text{ip}_1} \tag{26}$$

$$\Delta\phi_{\text{node}_1\to\text{ip}_1} = \nabla\phi_1.\mathbf{\Delta r}_{\text{node}_1-\text{ip}_1} \tag{27}$$

represent the main contributions of the new second-order MAW scheme. $\mathbf{\Delta r}_{\text{node}_1-\text{ip}_1}$ and $\mathbf{\Delta r}_{\text{node}_2-\text{ip}_1}$ are the distance vectors between integration point ip_1 and the nodes 1 and 2, respectively. $\mathbf{\Delta r}_{\text{ip}_1-\text{ip}_1}$ and $\mathbf{\Delta r}_{\text{ip}_3-\text{ip}_1}$ are the distance vectors between integration point ip_1 and the integration points 1 and 3, respectively. $\nabla\phi_1$ and $\nabla\phi_2$ are volume-averaged gradients of ϕ associated with the control volumes of nodes 1 and 2, respectively. For example, the

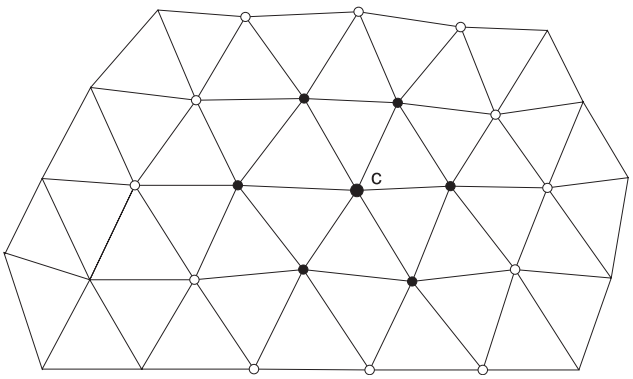

Figure 3. Node stencil.

volume-averaged gradient of ϕ associated with the control volume of node 1 (see Figure 1) is calculated using the following expression:

$$\nabla\phi_1 = \frac{1}{V_1}\int_{caod} (\nabla\phi)_{\text{ele}}\,\mathrm{d}V + (\text{Similar contributions from other elements associated with node 1}) \quad (28)$$

In this formula, V_1 is the volume of the control volume around node 1 and $(\nabla\phi)_{\text{ele}}$ is the gradient of ϕ at the element level computed by interpolating linearly ϕ in each element. Only the contributions from one triangular element (i.e. from the subcontrol volume **caod** in Figure 1) are presented explicitly in Equation (28). The contributions for the other elements associated with node 1 are determined in a similar manner by using an 'element-by-element' assembling procedure.

The original first-order MAW scheme involves only the values of ϕ at the nodes of the triangular element of interest. Consequently, the resulting node stencil for the discretized momentum equation of node **c** when using the original first-order MAW scheme involves the nodes of all the triangular elements having node **c** as one of their vertices (nodes identified by the full circle in Figure 3). In the proposed second-order MAW scheme, the contributions of the control-volume volume-averaged gradients of ϕ introduce additional nodes to the node stencil identified by the open circles in Figure 3.

The second-order contribution to the value of ϕ at the three integration points can be defined as the difference between the second-order and first-order values of ϕ at the integration points as follows:

$$\begin{aligned} \Delta\phi_{\text{ip}_1} &= \phi^{2\text{nd}}_{\text{ip}_1} - \phi_{\text{ip}_1} \\ \Delta\phi_{\text{ip}_2} &= \phi^{2\text{nd}}_{\text{ip}_2} - \phi_{\text{ip}_2} \\ \Delta\phi_{\text{ip}_3} &= \phi^{2\text{nd}}_{\text{ip}_3} - \phi_{\text{ip}_3} \end{aligned} \quad (29)$$

where ϕ_{ip_1}, ϕ_{ip_2} and ϕ_{ip_3} correspond to the values of ϕ at the integration points given by the original first-order MAW scheme when solving Equations (18).

Subtracting Equation (16) from Equation (23) and using the definitions of the second-order contribution to the value of ϕ at the three integration points (see Equation (29)) yields

$$\begin{aligned}\mathbf{\Delta}\phi_{\mathrm{ip}_1} = A_1.[f_{1_R}.(\mathbf{\Delta}\phi_{\mathrm{ip}_2} + \Delta\phi_{\mathrm{ip}_2\to\mathrm{ip}_1}) + (1 - f_{1_R}).\Delta\phi_{\mathrm{node}_2\to\mathrm{ip}_1}] \\ + (1 - A_1).[f_{1_L}.(\mathbf{\Delta}\phi_{\mathrm{ip}_3} + \Delta\phi_{\mathrm{ip}_3\to\mathrm{ip}_1}) + (1 - f_{1_L}).\Delta\phi_{\mathrm{node}_1\to\mathrm{ip}_1}]\end{aligned} \tag{30}$$

The weighting factors f_{1_R} and f_{1_L} determined by the ratio of mass fluxes coming from upwind nodes in Equation (23) remain unchanged, they are the same as in the original MAW scheme. This equation links together $\Delta\phi_{\mathrm{ip}_1}$, $\Delta\phi_{\mathrm{ip}_2}$, $\Delta\phi_{\mathrm{ip}_3}$—the unknown second-order contributions at the three integration points of the triangular element.

When the three equations for the three integration points of a triangular element are constructed, a system of three linear equations for three unknown $\Delta\phi_{\mathrm{ip}_1}$, $\Delta\phi_{\mathrm{ip}_2}$, $\Delta\phi_{\mathrm{ip}_3}$ is obtained

$$\begin{aligned}\mathbf{\Delta}\phi_{\mathrm{ip}_1} - A_1 f_{1_R}\mathbf{\Delta}\phi_{\mathrm{ip}_2} - (1 - A_1) f_{1_L}\mathbf{\Delta}\phi_{\mathrm{ip}_3} &= A_1[(1 - f_{1_R})\Delta\phi_{\mathrm{node}_2\to\mathrm{ip}_1}] \\ &\quad + (1 - A_1)[(1 - f_{1_L})\Delta\phi_{\mathrm{node}_1\to\mathrm{ip}_1}] \\ &\quad + A_1[f_{1_R}\Delta\phi_{\mathrm{ip}_2\to\mathrm{ip}_1}] \\ &\quad + (1 - A_1)[f_{1_L}\Delta\phi_{\mathrm{ip}_3\to\mathrm{ip}_1}] \\ -(1 - A_2) f_{2_L}\mathbf{\Delta}\phi_{\mathrm{ip}_1} + \mathbf{\Delta}\phi_{\mathrm{ip}_2} - A_2 f_{2_R}\mathbf{\Delta}\phi_{\mathrm{ip}_3} &= A_2[(1 - f_{2_R})\Delta\phi_{\mathrm{node}_3\to\mathrm{ip}_2}] \\ &\quad + (1 - A_2)[(1 - f_{2_L})\Delta\phi_{\mathrm{node}_2\to\mathrm{ip}_2}] \\ &\quad + A_2[f_{2_R}\Delta\phi_{\mathrm{ip}_3\to\mathrm{ip}_2}] \\ &\quad + (1 - A_2)[f_{2_L}\Delta\phi_{\mathrm{ip}_1\to\mathrm{ip}_2}] \\ -A_3 f_{3_R}\mathbf{\Delta}\phi_{\mathrm{ip}_1} - (1 - A_3) f_{3_L}\mathbf{\Delta}\phi_{\mathrm{ip}_2} + \mathbf{\Delta}\phi_{\mathrm{ip}_3} &= A_3[(1 - f_{3_R})\Delta\phi_{\mathrm{node}_1\to\mathrm{ip}_3}] \\ &\quad + (1 - A_3)[(1 - f_{3_L})\Delta\phi_{\mathrm{node}_3\to\mathrm{ip}_3}] \\ &\quad + A_3[f_{3_R}\Delta\phi_{\mathrm{ip}_1\to\mathrm{ip}_3}] \\ &\quad + (1 - A_3)[f_{3_L}\Delta\phi_{\mathrm{ip}_2\to\mathrm{ip}_3}]\end{aligned} \tag{31}$$

The solution of this system will yield $\Delta\phi_{\mathrm{ip}_1}$, $\Delta\phi_{\mathrm{ip}_2}$ and $\Delta\phi_{\mathrm{ip}_3}$—the contributions of the proposed second-order MAW scheme to the values of the transported variable ϕ at the three integration points ip_1, ip_2 and ip_3 in each triangular element.

The second-order mass-weighted averages of ϕ are assumed to prevail over each control surface when the surface integrals of the convection terms, Equation (4), are evaluated. Consequently, the convection contribution is simply expressed as

$$\int_a^o \mathbf{J}_{\mathrm{C}} \cdot \mathbf{n}\,\mathrm{d}A = -\dot{m}_{\mathrm{ip}_1}\phi_{\mathrm{ip}_1}^{\mathrm{2nd}} = -\dot{m}_{\mathrm{ip}_1}(\phi_{\mathrm{ip}_1} + \Delta\phi_{\mathrm{ip}_1}) \tag{32}$$

$$\int_o^d \mathbf{J}_{\mathrm{C}} \cdot \mathbf{n}\,\mathrm{d}A = \dot{m}_{\mathrm{ip}_3}\phi_{\mathrm{ip}_3}^{\mathrm{2nd}} = \dot{m}_{\mathrm{ip}_3}(\phi_{\mathrm{ip}_3} + \Delta\phi_{\mathrm{ip}_3}) \tag{33}$$

The algebraic approximation of the elemental convection contribution can be compactly expressed as follows:

$$\int_a^o \mathbf{J}_C \cdot \mathbf{n}\, dA + \int_o^d \mathbf{J}_C \cdot \mathbf{n}\, dA = C_1^\phi \phi_1 + C_2^\phi \phi_2 + C_3^\phi \phi_3 + D^\phi \tag{34}$$

The expressions for C_1^ϕ, C_2^ϕ, and C_3^ϕ in Equation (34) are exactly the same as those for the original MAW scheme appearing in Equation (21). However, a new contribution now appears, denoted D^ϕ, and expressed as

$$D^\phi = \dot{m}_{ip_3}.\Delta\phi_{ip_3} - \dot{m}_{ip_1}.\Delta\phi_{ip_1} \tag{35}$$

Expressions similar to Equation (34) can be derived for the convection contributions of all elements associated with the internal node **c** shown in Figure 2. Such expressions, when substituted into Equation (4), yield the complete convection contribution to the discretization equation for node **c** (Equation (5)).

To implement this second-order MAW scheme, a deferred correction approach [18] is adopted: the second-order contribution D^ϕ is treated explicitly and added to the source term in the right-hand side of the discretization equation for node **c**. Consequently, when using the proposed second-order MAW scheme, the influence coefficients remain the same as in the original MAW scheme. This contributes to the stability of the proposed solution procedure.

The similarity between the system of Equations (31) and the system shown in Equations (18) is obvious. Compared to Equations (18), all matrix coefficients in Equations (31) remain the same. Only the unknowns ϕ_{ip} in Equations (18) are replaced by $\Delta\phi_{ip}$. On the right-hand side, the values of ϕ_i at the integration points are replaced by $\Delta\phi_{ip}$, the second-order contributions. The second-order contributions $\Delta\phi_{ip}$ are computed in the same manner as are the values of ϕ at the integration points in the original MAW scheme. These second-order contributions follow the spirit of the skewed positive-influence coefficient upwind scheme proposed by Schneider and Raw [12] and will contribute positively to the influence coefficient. Since the second-order values of ϕ at the integration points, ϕ_{ip}^{2nd}, are the sum of two quantities computed using the positive influence-coefficient scheme of Schneider and Raw, namely ϕ_{ip} and $\Delta\phi_{ip}$, a stable system of discretization equations is obtained. Furthermore, the proposed second-order MAW scheme is not unidirectional but skewed, as is the original MAW scheme, which is more precise and more flexible than are unidirectional schemes [12].

In general, second-order schemes are less stable than first-order schemes so that limiters are needed to maintain numerical stability. These limiters restrict the second-order contributions when needed by applying multipliers (between 0 and 1) to the node gradients. This ensures that, there are no new extrema generated at integration points by the introduction of second-order terms [14]. The proposed second-order MAW scheme is very stable without the use of such conventional limiters. It is validated in the test cases carried out for the verification, where all calculations converged well without using conventional limiters. It is to be noted however that the mass-weighted second-order corrections $\Delta\phi_{ip}$ computed using Equations (31) contributes positively to the influence coefficients in the same spirit than the original MAW scheme. It may be considered as a form of continuous limiter, which is not constructed separately and used ocasionally like some conventional limiters, but is integrated in the construction of the proposed scheme.

6. VERIFICATION TESTS

6.1. Pure convection problem

To evaluate the difference in level of artificial viscosity between first- and second-order MAW schemes, a pure convection problem, where the diffusion coefficient of transported parameter is set equal to zero, is first analysed.

Since the velocity field is uniform and the diffusion coefficient is zero, the diffusion, if present in the discretized solution, is caused only by the artificial viscosity originating from truncation errors of the numerical scheme.

6.1.1. Shear layer. In the case of the shear layer problem, the computation domain is a $1\,\mathrm{m} \times 1\,\mathrm{m}$ square discretized with 441 nodes distributed uniformly (21 nodes $\times$ 21 nodes).

The uniform velocity field is not parallel to the main mesh directions, but parallel to the diagonal $y = x$, as illustrated in Figure 4 ($\mathbf{V} = 1\imath + 1\jmath$). A piecewise profile of temperature is imposed at the computational-domain inlets: $T = 400°\mathrm{C}$ on boundary $x = 0$ and $T = 200°\mathrm{C}$ on boundary $y = 0$. The discretized solutions were assumed to be converged when the sum of the absolute values of the non-dimensional residues were below 10^{-8}.

Figure 5 shows the temperature fields obtained with the first-order (top), FLO (middle) and second-order (bottom) schemes. The isotherms obtained with the second-order and FLO schemes are almost parallel to the flow direction, while the isotherms of the first-order scheme diverge strongly from the direction of the flow.

Figure 6 shows the temperature profiles obtained with four different schemes along the diagonal perpendicular to the flow direction ($x + y = 1$). They are compared with the exact discretized solution for this 21×21 uniform grid.

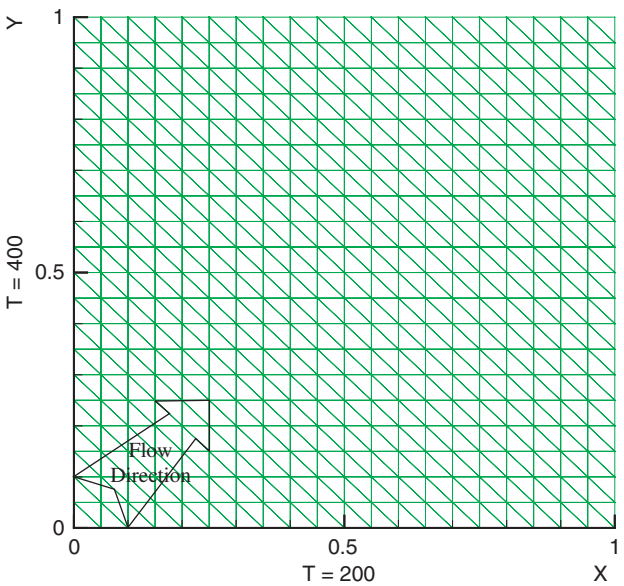

Figure 4. Mesh for pure convection shear layer.

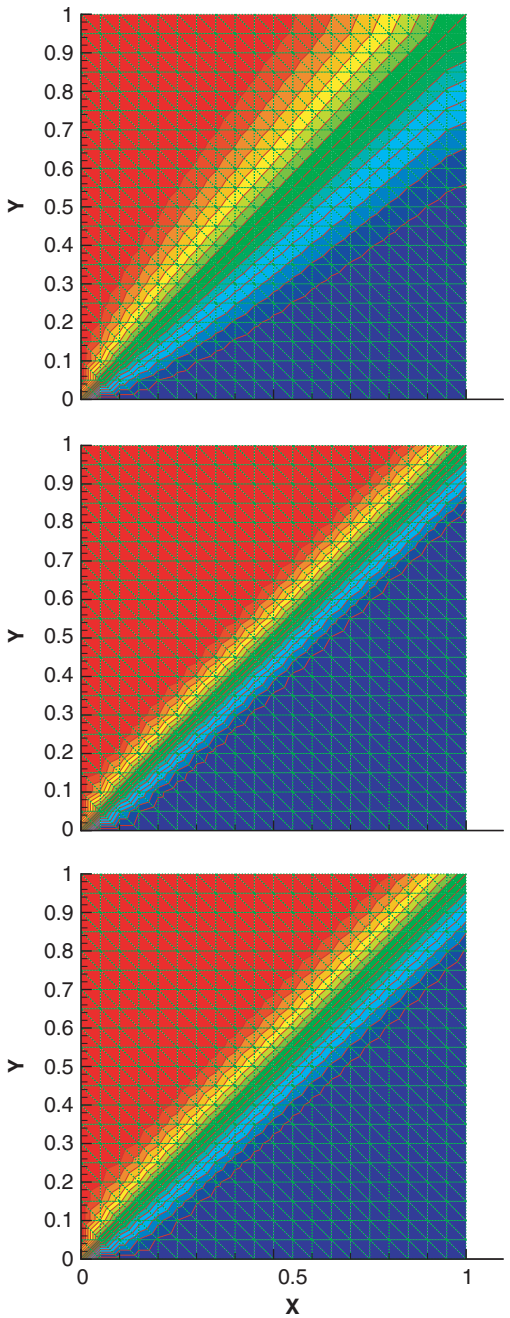

Figure 5. Shear layer: temperature fields obtained with original first-order MAW scheme (top), FLO scheme (middle) and new second-order MAW scheme (bottom).

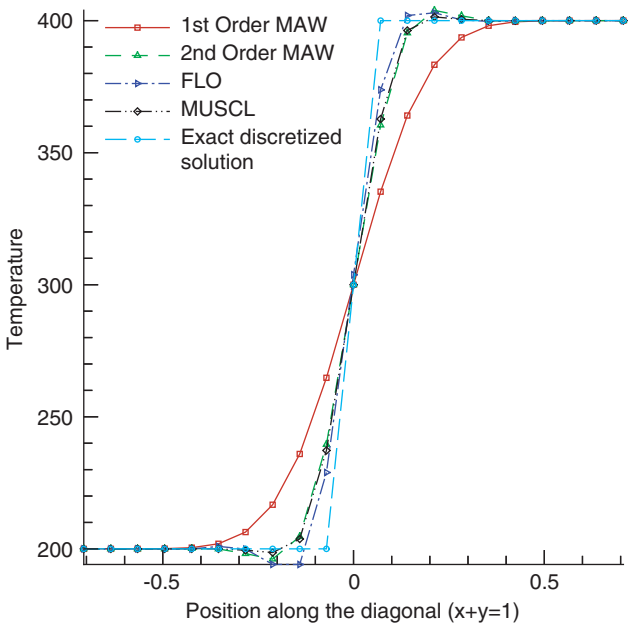

Figure 6. Shear layer: temperature profiles along the diagonal $(x + y = 1)$ perpendicular to the flow direction.

6.1.2. Convected front. In the case of the convected front problem, the computation domain is a $1\,\mathrm{m} \times 1\,\mathrm{m}$ square discretized with 1681 nodes distributed uniformly (21 nodes $\times$ 21 nodes).

The uniform velocity field is parallel to the main mesh directions ($\mathbf{V} = 1\imath$). Initially, the fluid temperature in the computational domain is set to 200°C. However, the fluid entering at the computational-domain inlet has a temperature of 100°C while adiabatic boundary conditions are applied on boundaries $y = 0$ and $y = 1\,\mathrm{m}$. With such boundary conditions, it is clear that the exact solution corresponds to a convected front which can be expressed as follows:

$$T(x, y, t) = \begin{cases} 100 & \text{if } x \leqslant |\mathbf{V}|t \\ 200 & \text{if } x > |\mathbf{V}|t \end{cases} \tag{36}$$

In this unsteady case, the discretized solutions at a given time step were assumed to be converged when the sum of the absolute values of the non-dimensional residues were below 10^{-8}. A time-step size of 0.01 s was used for this problem.

Figure 7 shows the temperature profiles obtained with four different schemes along the horizontal centreline ($x = \frac{1}{2}$) at $t = 0.5\,\mathrm{s}$. They are compared with the exact discretized solution for this 41×41 uniform grid.

From the results of these two simple pure convection problems, it is clear that the proposed second-order MAW scheme considerably reduces the influence of artificial viscosity with respect to the original first-order MAW scheme and reaches the MUSCL scheme's level of accuracy.

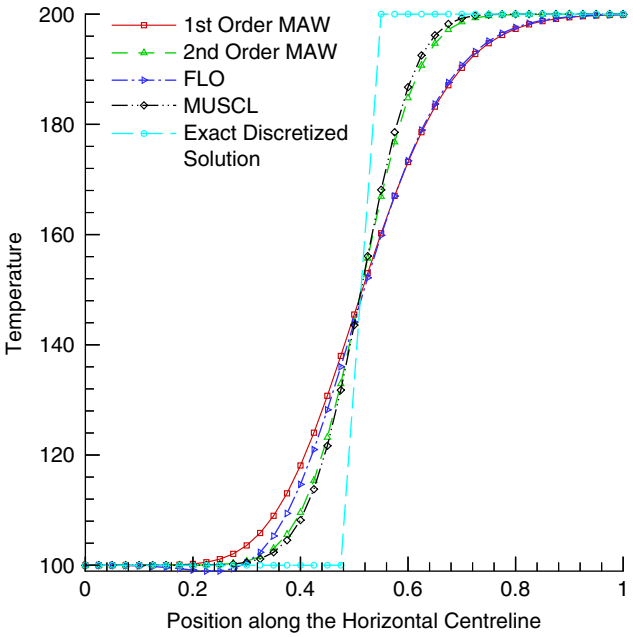

Figure 7. Convecting front: temperature profiles along horizontal centreline at $t = 0.5$ s.

6.2. *Driven cavity*

The classical 2D square-driven cavity problem $0 \leqslant x \leqslant L,\ 0 \leqslant y \leqslant L$ with $u(x, L) = U_{\text{wall}}$ is used to demonstrate the performance of the proposed second-order MAW scheme (see Figure 8). To qualify the accuracy of the proposed formulation, calculations have been performed on three different uniform grids using the MAW, MUSCL and FLO schemes. The discretized solutions were assumed to be converged when the sum of the absolute values of the non-dimensional residues were below 10^{-8}. Convergence histories down to machine precision acheived by these schemes are presented in Figure 9. Table I compares values of minimal and maximal centreline velocities at $Re = 400$. The Reynolds number for this problem has been defined as $Re = \rho U_{\text{wall}} L/\mu$. The relative errors, calculated with respect to the benchmark solution of Ghia *et al.* [19], show the second-order accuracy of both the proposed second-order MAW and the MUSCL schemes (see Figure 10).

Using the second-order MAW scheme, the proposed CVFEM yields results that are in good agreement with the benchmark calculations made by Ghia *et al.* [19]. However, the MAW scheme computations systematically display lower accuracy, confirming the observations of Saabas *et al.* [1, 5].

6.3. *Flow over a circular cylinder*

Laminar incompressible flow around a circular cylinder is a classical problem and is well documented in the literature. To accurately simulate this phenomenon, it is essential to employ a high-accuracy discretization scheme. This problem is consequently a good validation test for the proposed second-order MAW scheme.

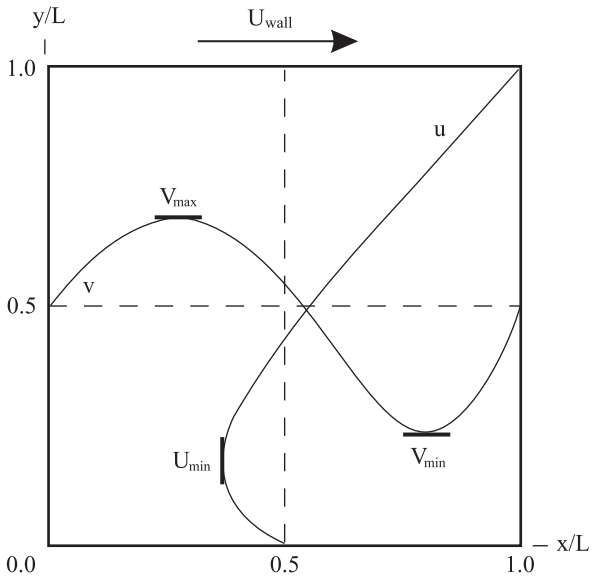

Figure 8. Definitions for lid-driven cavity flows.

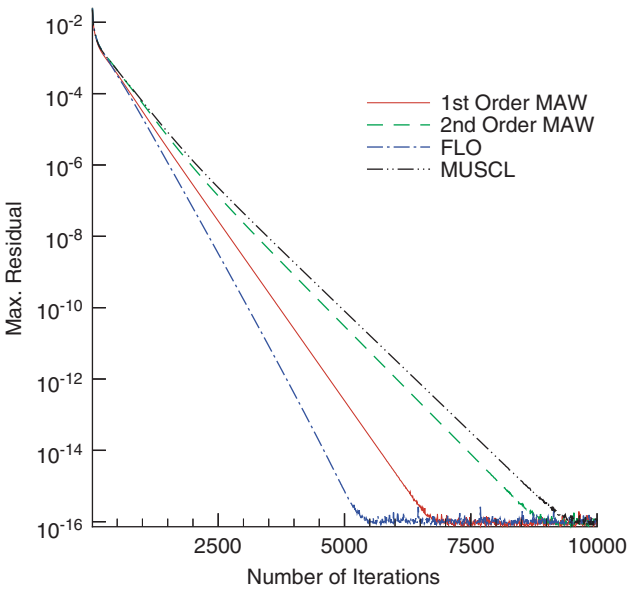

Figure 9. Lid-driven cavity: convergence history.

At low Reynolds numbers ($Re < 40$), the flow field over the cylinder is stationary and is characterized by the presence of a pair of symmetric vortices. At higher Reynolds numbers, the flow becomes unsteady, asymmetric and alternate vortex shedding occurs behind the cylinder.

Table I. Lid-driven cavity: maximum and minimum centreline velocities-$Re = 400$.

Scheme	Grid	$\frac{U_{min}}{U_{\text{wall}}}$ (rel. error)	$\frac{V_{min}}{U_{\text{wall}}}$ (rel. error)	$\frac{V_{max}}{U_{\text{wall}}}$ (rel. error)	Average rel. error
MAW	32×32	−.20729 (−36.6%)	−.33468 (−25.6%)	.20237 (−33.0%)	31.7%
MAW 2nd order		−.33513 (2.4%)	−.46982 (4.4%)	.31478 (4.2%)	3.7%
FLO		−.25841 (−21.0%)	−.37622 (−16.4%)	.24042 (−20.4%)	19.3%
MUSCL		−.33286 (1.7%)	−.43728 (−2.8%)	.31279 (3.6%)	2.7%
MAW	64×64	−.24827 (−24.1%)	−.37509 (−16.6%)	.23567 (−22.0%)	20.9%
MAW 2nd order		−.33104 (1.1%)	−.45829 (1.9%)	.30680 (1.6%)	1.5%
FLO		−.30192 (−7.8%)	−.42476 (−5.6%)	.27823 (−7.9%)	7.1%
MUSCL		−.32966 (.7%)	−.44540 (−1.0%)	.30656 (1.5%)	1.1%
MAW	128×128	−.28012 (−14.4%)	−.40763 (−9.4%)	.26206 (−13.2%)	12.3%
MAW 2nd order		−.32703 (−.1%)	−.45202 (.5%)	.30028 (−.6%)	.4%
FLO		−.32052 (−2.1%)	−.44475 (−1.1%)	.29548 (−2.2%)	1.8%
MUSCL		−.32800 (.2%)	−.45169 (.4%)	.30287 (−.3%)	.3%
Ghia [19]	129×129	−.3273 (0%)	−.4499 (0%)	.3020 (0%)	0%

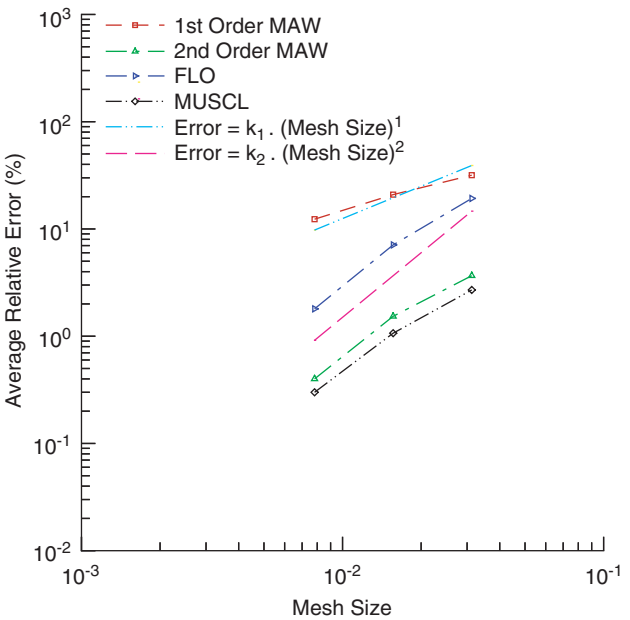

Figure 10. Lid-driven cavity: grid-resolution study.

The vortex generation period, characterized by its Strouhal number, depends on the Reynolds number.

This flow problem shows the ability of the proposed second-order MAW scheme to accurately predict flow structure, reattachment length and the Strouhal number by comparing predictions against experimental results.

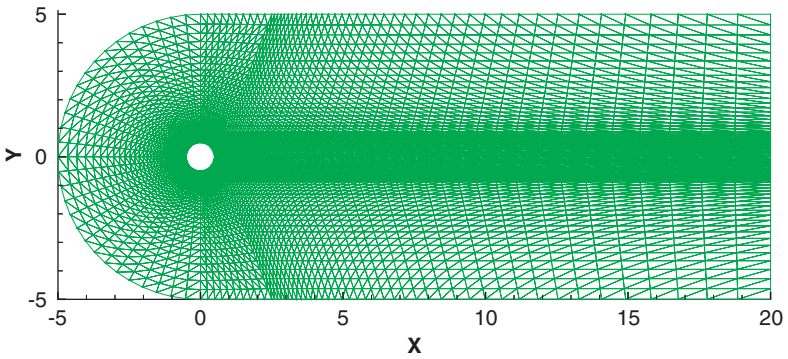

Figure 11. Mesh for the calculation of flow around the circular cylinder.

6.3.1. Mesh. An unstructured mesh based on triangular elements is used in the entire calculation domain (Figure 11). It is composed of 5500 nodes and is perfectly symmetric around the centre line. In the cases of steady flows occurring at low Reynolds numbers, before the occurrence of vortex shedding, the solution is symmetric. A symmetric mesh was chosen because it is a necessary condition to obtain a perfectly symmetric solution, which then served as one of the criteria for verifying the implementation of the proposed scheme.

The domain width is about 10 times the cylinder diameter D ($D = 1\,\mathrm{m}$) and its length is about $5D$ upstream and $20D$ downstream.

6.3.2. Specified conditions. The inlet includes a semi-circle at the left and also two horizontal boundaries above and below the computational domain. At these inlets, the velocity is set to a value of $1\,\mathrm{m/s}$ parallel to x-axis. At the outlet (the right vertical boundary), the manometric pressure is imposed equal to zero. The fluid density is $1\,\mathrm{kg/m^3}$ and the viscosity μ is specified in such a way as to obtain the desired Reynolds number.

To simulate an unsteady flow over a circular cylinder, a perturbation must be introduced into the flow at the beginning of the simulation. The nature of this initial perturbation does not influence the flow characteristics [20]. In this paper, the flow perturbation has been introduced simply by imposing an asymmetric velocity profile at the beginning of the simulation, and by running it briefly, for example during 1–2 vortex shedding periods, and then continuing with the normal symmetric boundary conditions described above.

6.3.3. Reattachment length at a low Reynolds number. At $Re \leqslant 40$, the flow is steady with two symmetric vortices attached behind the cylinder. The reattachment length L is measured from the downstream side of the cylinder to the point on the centre line where the x velocity component reaches a value of zero. The discretized solutions were assumed to be converged when the sum of the absolute values of the non-dimensional residues were below 10^{-8}. Convergence histories down to machine precision acheived by these schemes are presented in Figure 12.

The relative reattachment length, L/D, depends on the number. At $Re = 40$, the experimental value of L/D is about 2.2 [20]. Because of the high rate of the artificial artificial viscosity,

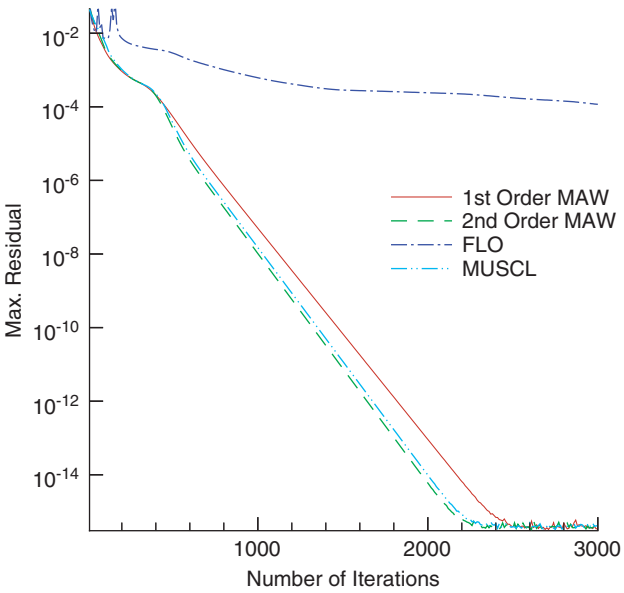

Figure 12. Circular cylinder: convergence history.

the original first-order MAW scheme underestimates L/D, as approximately 1.8 (Figure 13, top). The proposed second-order MAW scheme L/D, around 2.2 (Figure 13, bottom).

6.3.4. Period of vortex shedding in the unsteady flow at a high Reynolds number. When the Reynolds number is higher than 40, the flow regime becomes unsteady. At $Re = 100$, the Von-Karman street behind the cylinder is well defined (see Figure 14) with a fixed vortex shedding frequency f. In this unsteady case, the discretized solutions at a given time step were assumed to be converged when the sum of the absolute values of the non-dimensional residues were below 10^{-8}. A time-step size of 0.1 s was used for this problem. The experimental value of the corresponding Strouhal number ($St = D.f/U_\infty$) at $Re = 100$ is 0.165 [20, 21], corresponding to a vortex shedding period T of 6.06 s. The proposed second-order MAW scheme gives a fairly good value of $T \approx 6.0$ s (cf. Figure 15, right), corresponding to a Strouhal number of 1.66. The vortex shedding is strongly damped when using the first-order MAW scheme (cf. Figure 15, left).

6.4. Summary

In comparison with the first-order MAW scheme, the proposed second-order MAW scheme does not need more computer memory and the convergence is achieved practically with the same amount of iterations. The proposed scheme is more precise and generates less artificial viscosity than the original first-order MAW scheme. It is also as stable as the first-order MAW scheme and can converge even on grids having elements with obtuse angles, where the accurate FLO scheme, is certain to diverge. Consequently, the proposed second-order MAW scheme produced a more precise solution than the original first-order MAW scheme with the same amount of computer resources (memory and CPU time).

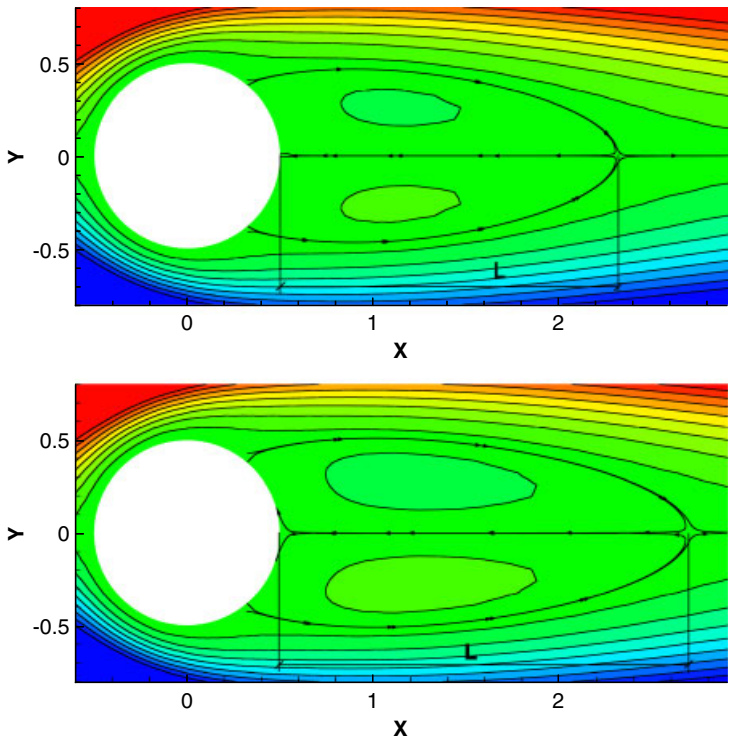

Figure 13. Streamlines behind the cylinder at $Re = 40$: first-order MAW scheme solution (top), second-order MAW scheme solution (bottom).

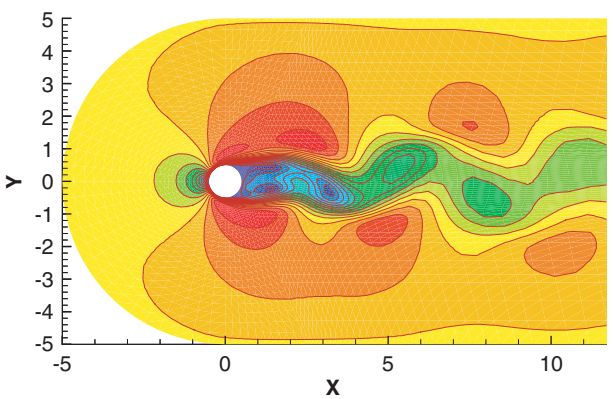

Figure 14. Absolute velocity contour around the cylinder at $Re = 100$—second-order MAW scheme.

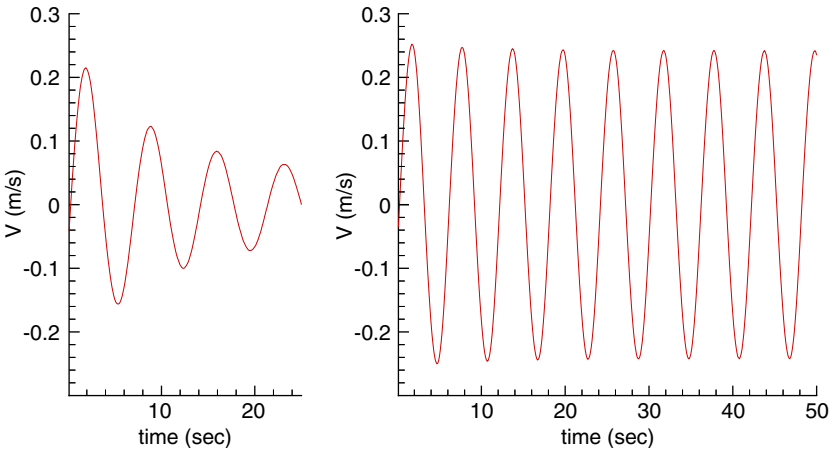

Figure 15. Transversal velocity at a point on centre line behind a circular cylinder in the unsteady flow at $Re = 100$. First-order MAW scheme: decaying velocity amplitude (left); second-order MAW scheme: constant velocity amplitude (right).

7. CONCLUSIONS

A new second-order scheme for convection terms, based on the original first-order MAW scheme, has been developed, implemented and validated in this paper.

Compared to the original first-order MAW scheme, the new scheme exhibits less artificial viscosity and yields excellent results in the test cases of a pure convection problem, and steady and unsteady flows over a circular cylinder.

Furthermore, the new second-order MAW scheme inherits the well-known stability characteristics of the original first-order scheme. In the five test cases carried out for the validation of this new scheme, calculations were converged without the use of limiters. This is in clear contrast to the second-order scheme available in the literature.

In general, when the flow direction is aligned with the grid, first-order upwind discretizations are acceptable. However, when the flow is no longer aligned with the grid, first-order upwind discretizations exhibit large discretization errors. Since the flow direction is generally not aligned with the grid in unstructured meshes, numerical results are more accurate when second-order formulations are used, especially for complex configurations. The proposed second-order MAW scheme, with its accuracy and high stability, is therefore well suited for complex flow configuration.

ACKNOWLEDGEMENTS

This study has received support from the Canada Research Chair Program, the *Ministère des ressources naturelles du Québec* through its *Programme d'aide au développement des technologies de l'énergie*, and the Canadian Natural Resources Ministry through its Efficiency and Alternative Energy Program. Support from the Natural Sciences and Engineering Research Council of Canada (NSERC) in the form of research grants is gratefully acknowledged.

REFERENCES

1. Baliga BR, Patankar SV. A new finite element formulation for convection–diffusion problems. *Numerical Heat Transfer* 1980; **3**:393–409.
2. Prakash C. An improved control volume finite element method for heat and mass transfer and for fluid flow using equal order velocity–pressure interpolation. *Numerical Heat Transfer* 1985; **8**:259–280.
3. Prakash C, Patankar SV. A control-volume based finite element method for solving the Navier–Stokes equations using equal-order velocity–pressure interpolation. *Numerical Heat Transfer* 1986; **9**:253–276.
4. Saabas HJ, Baliga BR. Co-located equal-order control-volume finite-element method for multidimensional, incompressible, fluid flow—Part I. *Numerical Heat Transfer* 1994; **26B**:381–407.
5. Masson C, Saabas HJ, Baliga BR. Co-located equal-order control-volume finite element method for two-dimensional axisymmetric incompressible fluid flow. *International Journal for Numerical Methods in Fluids* 1994; **18**:1–26.
6. Reyes M, Rincon J, Damia J. Simulation of turbulent flow in irregular geometries using a control-volume finite-element method. *Numerical Heat Transfer Part B-Fundamentals* 2001; **39**(1):79–89.
7. Chiu HT, Lee LJ. Simulation of liquid composite molding based on control-volume finite element method. *Journal of Polymer Engineering* 2002; **22**(3):155–176.
8. Stry Y, Hainke M, Jung T. Comparison of linear and quadratic shape functions for a hybrid control-volume finite element method. *International Journal of Numerical Methods for Heat and Fluid Flow* 2002; **12**(8):1009–1031.
9. Turki S, Abbassi H, Nasrallah SB. Effect of the blockage ratio on the flow in a channel with a built-in square cylinder. *Computational Mechanics* 2003; **33**(1):22–29.
10. Turki S, Abbassi H, Ben Nasrallah S. Two-dimensional laminar fluid flow and heat transfer in a channel with a built-in heated square cylinder. *International Journal of Thermal Sciences* 2003; **42**(12):1105–1113.
11. Ammara I, Masson C. Development of a fully coupled control-volume finite element method for the incompressible Navier–Stokes equations. *International Journal for Numerical Methods in Fluids* 2004; **44**:621–644.
12. Schneider GE, Raw MJ. A skewed positive influence coefficient upwinding procedure for control volume base finite element convection diffusion computation. *Numerical Heat Transfer* 1986; **9**:1–26.
13. Leonard BP, Drummond JE. Why you should not use 'hybrid', 'power law' or related exponential schemes for convective modeling—there are much better alternatives. *International Journal for Numerical Methods in Fluids* 1995; **20**:421–442.
14. Barth TJ, Jespersen DC. The design and application of upwind schemes on unstructured meshes. *AIAA-89-0366*, 1998.
15. Frink NT. Upwind scheme for solving the Euler equation on unstructured triangular meshes. *AIAA Journal* 1991; **29**:1619–1626.
16. Rhie CM, Chow WL. Numerical study of the turbulent flow past an airfoil with trailing edge separation. *AIAA Journal* 1983; **21**:1525–1532.
17. Smaïli A, Masson C. Aerodynamic analysis of rotor—nacelle interaction for wind turbines. *2002 Canadian CFD Annual Conference*, 2002; 546–552.
18. Khosla PK, Rubin SG. A diagonally dominant second-order accurate implicit scheme. *Computers and Fluids* 1974; **2**:207–209.
19. Ghia U, Ghia KN, Shin CT. High-Re solution for incompressible flow using the Navier–Stokes equation and multigrid method. *Journal of Computational Physics* 1982; **48**:387–411.
20. Braza M, Chassaing P, Minh HH. Numerical study and physical analysis of the pressure and velocity fields in the near wake of a circular cylinder. *Journal of Fluid Mechanics* 1986; **165**(Part 4):79–130.
21. Li J, Chambarel A, Donneaud M, Martin R. Numerical study of laminar flow past one and two cylinders. *Computers and Fluid* 1991; **19**:155–170.

